

The fast committor machine: Interpretable prediction with kernels

D. Aristoff,¹ M. Johnson,¹ G. Simpson,² and R. J. Webber³

¹*Mathematics, Colorado State University, USA^a*

²*Mathematics, Drexel University, USA*

³*Computing & Mathematical Sciences, California Institute of Technology, USA*

In the study of stochastic dynamics, the committor function describes the probability that a process starting from an initial configuration x will reach set A before set B . This paper introduces a fast and interpretable method for approximating the committor, called the “fast committor machine” (FCM). The FCM is based on simulated trajectory data, and it uses this data to train a kernel model. The FCM identifies low-dimensional subspaces that optimally describe the A to B transitions, and the subspaces are emphasized in the kernel model. The FCM uses randomized numerical linear algebra to train the model with runtime that scales linearly in the number of data points. This paper applies the FCM to example systems including the alanine dipeptide miniprotein: in these experiments, the FCM is generally more accurate and trains more quickly than a neural network with a similar number of parameters.

I. INTRODUCTION

Many physical systems exhibit metastability, which the tendency to occupy a region A of phase space for a comparatively long time before a quick transition to another region B . Metastability is especially common in molecular dynamics, where states A and B might correspond to the folded and unfolded conformations of a protein. Metastability also arises in continuum mechanics¹, biological systems², fluids³, and the Earth’s climate⁴.

To gain insight into high-dimensional metastable systems, it is necessary to numerically simulate and then analyze of the transition paths from state A to state B . The transition paths can be simulated by a variety of methods including transition path sampling^{5,6}, forward flux sampling^{7,8}, the string method^{9,10}, and adaptive multilevel splitting¹¹. In the rest of this work, assume that a data set of discrete-time trajectories has already been generated, which includes one or more transitions between A and B .

To analyze the transitions from A to B , scientists often evaluate the (forward) committor function^{3,4,12–17}, which measures the probability that the system starting at state x will reach B before A , thus making a transition. In symbols, the committor is given by

$$q^*(x) = \mathbb{P}_x(T_B < T_A), \quad (1)$$

where T_A and T_B are the first hitting times for A and B .

To numerically approximate the committor function, the trajectory data needs to be combined with an appropriate machine learning method. There are various machine learning methods available, including neural networks^{12,15,18}, diffusion maps¹⁶, and other tools¹³. As shortcomings, these methods can be slow to apply to large data sets (diffusion maps) or difficult to interpret (neural nets).

This work describes a new method for calculating committors called the fast committor machine (FCM), which is both efficient and interpretable. The FCM approximates the committor q^* using a linear combination of kernel functions, as follows:

- The recursive feature machine (RFM¹⁹) makes an adaptively chosen linear transformation of the phase space based on the estimated gradients of the target function. The RFM leads to an explicit, interpretable kernel function.
- Randomly pivoted Cholesky (RPC²⁰) optimizes the coefficients used in the kernel approximation. RPC is a randomized linear algebra approach that processes N data points using just $\mathcal{O}(N)$ floating point operations and $\mathcal{O}(N)$ storage.

Both strategies were introduced recently in 2022 and appear to be new in the chemical physics literature.

The fast committor machine combines these strategies, yielding superior performance in experiments: the method is generally more accurate and trains more quickly than a neural network with a similar number of parameters. As another advantage, the FCM is interpretable, revealing low-dimensional linear subspaces that optimally describe the transition pathways from A to B .

In summary, the FCM is a method for approximating the committor, which is based making an adaptively chosen linear transformation of the phase space. As extensions to this work, piecewise linear or fully nonlinear transformations might further enhance the accuracy of the method. Nonetheless, the FCM is competitive in experiments, and it represents an important step forward in the development of efficient, interpretable committor methods.

A. Relationship to past work

Kernel method have been frequently applied for force field calculations in materials science²¹. Yet there is wide acknowledgment that the efficiency of kernel methods depends on finding a suitable distance function between different molecular configurations²².

Two distances are currently being advocated in the chemical physics literature. Both could be used with kernels. Diffusion maps²³ provide a sophisticated distance function that adapts to the nonlinear manifold structure in the input data. Diffusion maps have recently been used to approximate the committor¹⁶. Alternately, the variational approach

^a) Author to whom correspondence should be addressed: aristoff@colostate.edu

to conformational dynamics (VAC²⁴) identifies a coordinate transformation that amplifies slowly decorrelating dynamical modes and suppresses quickly decorrelating dynamical modes. VAC is often used to help visualize and construct committor estimates^{25–27}.

A limitation of both diffusion maps and VAC is that they do not specifically target the sets A and B used in the committor. Therefore, greater accuracy could be potentially obtained by modifying the distance based on A and B definitions. This modification requires a fully adaptive learning strategy that redefines the kernel distance for each committor problem.

The kernel machine learning literature has proposed a different, flexible approach to distance construction. Many authors apply a *linear* transformation to their data before calculating a standard kernel based the Euclidean distance^{28,29}. The linear map can be adapted to the input data and also to the specific approximation task^{30,31}. A 2022 paper¹⁹ introduced the *recursive feature machine* (RFM), which constructs the linear feature map based on the estimated gradients of the target function. To justify the RFM, the authors compared the linear map with the first layer of a neural net, and they showed empirical and theoretical similarities. In experiments, they applied the RFM to RGB images with as many as 96×96 pixels, hence $96 \times 96 \times 3 = 27,648$ dimensions. They found that the RFM suppresses irrelevant directions and emphasizes important directions, which is especially important in high dimensions.

The RFM provides the template for a kernel-based approximation of the committor. Yet optimizing the coefficients in the kernel approximation remains computationally demanding. A naive optimization would require $\mathcal{O}(N^3)$ operations and $\mathcal{O}(N^2)$ storage, which is prohibitively expensive for $N \geq 10^5$ data points. The high computational cost of kernel methods has been described as a fundamental limitation in the past³². Nonetheless, modern strategies in randomized numerical linear algebra are leading to dramatic speed-ups^{20,33,34}.

This work applies randomly pivoted Cholesky (RPC²⁰) to speed up the kernel optimization and extend our experiments to $N = 10^6$ data points. To achieve these speed-ups, RPC generates a randomized rank- r approximation of the kernel matrix, where r is a parameter chosen by the user. The coefficients can be optimized in just $\mathcal{O}(Nr^2)$ operations and $\mathcal{O}(Nr)$ storage. For the experiments in Sec. III, a constant value of $r = 1000$ yields nearly converged committor results.

B. Outline for the paper

The rest of the paper is organized as follows. Section II describes the new FCM method for calculating the committor, Section III presents numerical experiments, and Section IV offers concluding remarks. Technical derivations are in Appendices A and B.

TABLE I: Definitions of symbols used in this work.

Symbol	Definition
\mathbf{x}, \mathbf{x}'	system states
A, B	initial and target sets
Ω	complement of $A \cup B$
$\mathbf{x}(t)$	underlying stochastic process
τ	lag time
$q^*(\mathbf{x})$	exact committor
θ	linear coefficients in kernel approximation
$q_\theta(\mathbf{x})$	estimated committor
$k_M(\mathbf{x}, \mathbf{x}')$	kernel function
M	scaling matrix
K	kernel matrix
I	identity matrix
$(\mathbf{x}_n, \mathbf{y}_n)$	time lagged pairs, $\mathbf{x}(0) = \mathbf{x}_n, \mathbf{x}(\tau) = \mathbf{y}_n$
N	number of training samples
μ	equilibrium density
ρ	sampling density
$w_n = \mu(\mathbf{x}_n)/\rho(\mathbf{x}_n)$	weight or likelihood of \mathbf{x}_n
$1_A, 1_B, 1_\Omega$	characteristic functions of A, B, Ω
ε	bandwidth parameter
γ	regularization parameter

C. Assumptions and notation

The FCM can be applied to any time-reversible process $\mathbf{x}(t) \in \mathbb{R}^d$ which has a discrete time step τ and equilibrium density μ . See Table I for a list of symbols and definitions.

II. NEW FCM METHOD FOR CALCULATING THE COMMITTOR

This section describes the new method for calculating the committor function q^* , called the “fast committor machine” (FCM).

A. Motivating variational principle

The FCM is motivated by a variational principle which states that the committor $q^*(\mathbf{x}) = \mathbb{P}_\mathbf{x}(T_B < T_A)$ is the unique minimizer of

$$\mathcal{L}(q) = \mathbb{E}_\mu |q(\mathbf{x}(0)) - q(\mathbf{x}(\tau))|^2, \quad (2)$$

among functions q satisfying $q = 0$ on A and $q = 1$ on B . The expectation \mathbb{E}_μ is averaging over all trajectories $\mathbf{x}(t)$ that are started from the equilibrium density $\mathbf{x}(0) \sim \mu$ and advanced forward to an end point $\mathbf{x}(\tau)$.

The quantity (2) is called the Dirichlet form associated with the Markov process, and it provides a popular cost function used for committor estimation in machine learning. Many works use a continuous-time version of the Dirichlet form^{12,15,35}, but the quantity (2) is the discrete-time version^{25,27}. The history and properties of the Dirichlet form are described in several pedagogical mathematical works^{36–38}.

To make practical use of the variational principle, the Dirichlet form needs to be approximated from data. Assume

that the data consists of N pairs $(\mathbf{x}_n, \mathbf{y}_n)_{n=1,2,\dots,N}$. The start point \mathbf{x}_n is randomly sampled from a density ρ . The end point \mathbf{y}_n is derived from running the process forward for τ time units starting from $\mathbf{x}(0) = \mathbf{x}_n$. Then, a data-driven approximation for $\mathcal{L}(q)$ is the weighted average

$$L(q) = \frac{1}{N} \sum_{n=1}^N w_n |q(\mathbf{x}_n) - q(\mathbf{y}_n)|^2, \quad (3)$$

where the weights are the likelihood ratios between the sampling density ρ and the target density μ :

$$w_n = \frac{\mu(\mathbf{x}_n)}{\rho(\mathbf{x}_n)}. \quad (4)$$

The weighted average (3) has a nice mathematical justification. If the data pairs $(\mathbf{x}_n, \mathbf{y}_n)_{n=1,2,\dots}$ are ergodic and ρ is *absolutely continuous*,

$$\rho(\mathbf{x}) > 0 \quad \text{whenever} \quad \mu(\mathbf{x}) > 0,$$

then the estimator (3) is unbiased

$$\mathbb{E}[L(q)] = \mathcal{L}(q),$$

and the law of large numbers guarantees $L(q) \rightarrow \mathcal{L}(q)$ as $N \rightarrow \infty$. Nonetheless, consistent with the law of large numbers, the accuracy of the weighted average may depend on generating a large quantity of data.

When the goal is variational minimization of $L(q)$, it is fine to work with alternative weights

$$w'_n = c \frac{\mu(\mathbf{x}_n)}{\rho(\mathbf{x}_n)},$$

where the multiplicative constant $c > 0$ can be chosen based e.g. on numerical stability. This makes the method applicable when the likelihood ratios are only known up to a constant multiplicative factor. For example, one sampling strategy is to raise the temperature of molecular dynamics simulations to facilitate greater phase space coverage (see the example in Sec. III B). Then, the relative weights are known but the absolute weights are typically unknown.

B. Form of the committor approximation

This paper proposes a new committor approximation that takes the form $q_\theta = 0$ on A , $q_\theta = 1$ on B , and

$$q_\theta(\mathbf{x}) = \sum_{n=1}^N \theta_n [k_M(\mathbf{x}_n, \mathbf{x}) - k_M(\mathbf{y}_n, \mathbf{x})], \quad \mathbf{x} \in \Omega. \quad (5)$$

In this definition, $\Omega = (A \cup B)^c$ is the region separate from A and B . Also, $\theta \in \mathbb{R}^N$ is a vector of real-valued coefficients, and

$$k_M(\mathbf{x}, \mathbf{x}') = \begin{cases} \exp(-\frac{1}{\varepsilon} \|M^{1/2}(\mathbf{x} - \mathbf{x}')\|), & \mathbf{x}, \mathbf{x}' \in \Omega \\ 0, & \text{otherwise} \end{cases} \quad (6)$$

is a bivariate kernel function with a bandwidth parameter $\varepsilon > 0$ and a positive definite scaling matrix $M \in \mathbb{R}^{d \times d}$.

The approximation q_θ is more succinct and empirically more accurate than alternative kernel-based parametrizations considered in Appendix A. By construction, q_θ satisfies the appropriate boundary conditions. Also, q_θ changes flexibly in the interior region Ω by varying the coefficients θ_n and shape parameters M and ε . Note that the kernel $k_M(\mathbf{x}, \mathbf{y})$ is not differentiable at $\mathbf{x} = \mathbf{y}$, but this paper uses $\nabla_{\mathbf{y}} k_M(\mathbf{x}, \mathbf{y}) = \mathbf{0}$ as the pseudogradient.

The rest of this section describes the FCM approach for optimizing the scaling matrix M , the coefficients θ , and the bandwidth ε .

C. Optimization of the scaling matrix M

The FCM incorporates a scaling matrix $M \in \mathbb{R}^{d \times d}$, which transforms the state variable $\mathbf{x} \in \mathbb{R}^d$ according to $\mathbf{x} \mapsto M^{1/2}\mathbf{x}$. The optimization of this scaling matrix is key to the performance of the FCM.

Researchers since the early 2000s have been combining kernels with a scaling matrix chosen as the inverse covariance matrix of the input data points^{28,29}. This choice of M transforms the data points so they are isotropic. However, for a long time it was unclear what other ways M could be optimized for kernel learning.

In 2022, researchers introduced a new approach for tuning the scaling matrix, called the ‘‘recursive feature machine’’ (RFM)^{19,39}. The RFM is a generalized kernel method that takes input/output pairs $f(\mathbf{x}_n) = b_n$ and iteratively learns both a regressor

$$f_\theta(\mathbf{x}) = \sum_{n=1}^N \theta_n k_M(\mathbf{x}_n, \mathbf{x}) \quad (7)$$

and a scaling matrix M . The method alternates between two steps:

- Update the coefficients θ_n so that f_θ minimizes the least-squares loss

$$\ell(f_\theta) = \frac{1}{N} \sum_{n=1}^N |f_\theta(\mathbf{x}_n) - b_n|^2$$

using the current scaling matrix M ;

- Update the scaling matrix

$$M = \sum_{n=1}^N \nabla f_\theta(\mathbf{x}_n) \nabla f_\theta(\mathbf{x}_n)^T. \quad (8)$$

using the current regressor f_θ .

The method iterates until finding an approximate fixed point for f_θ and M , and typically 3 – 6 iterations are enough¹⁹.

A complete analysis of the RFM lies beyond the scope of the current work. However, as an intuitive explanation, the linear transformation improves the ‘‘fit’’ between the target

Algorithm 1: Fast committor machine

Data: Training points: $(\mathbf{x}_n, \mathbf{y}_n, w_n)_{n=1, \dots, N}$; ;
 Solution vector: \mathbf{b} ;
 Kernel function: k ;
 Parameters: bandwidth ε , regularization γ , approximation rank r (multiple of 10);
Result: Scaling matrix M , committor estimate q_θ ;
 $M \leftarrow \mathbf{I}$;
 // Initialize M
 for $t = 1, \dots, 5$ do
 $M \leftarrow M / \text{tr cov}(\{M^{1/2}\mathbf{x}_1, \dots, M^{1/2}\mathbf{x}_N\})$;
 // Rescale M
 $k_{mn} \leftarrow k_M(\mathbf{x}_m, \mathbf{x}_n) - k_M(\mathbf{x}_m, \mathbf{y}_n) - k_M(\mathbf{y}_m, \mathbf{x}_n) + k_M(\mathbf{y}_m, \mathbf{y}_n)$;
 // Repopulate K with kernel k_M
 $k_{mn} \leftarrow \sqrt{w_m w_n} k_{mn}$;
 // Reweight K
 $S = \{s_1, \dots, s_r\} \leftarrow \text{RPCholesky}(K, r)$;
 // Apply Alg. 2
 $K(S, S) \leftarrow K(S, S) + \varepsilon_{\text{mach}} \text{tr}(K(S, S)) \mathbf{I}$;
 // Regularize
 $\boldsymbol{\eta} \leftarrow$ Solution to
 $[K(:, S)^T K(:, S) + \gamma N K(S, S)] \boldsymbol{\eta} = K(:, S)^T \mathbf{b}$;
 // Optimize coefficients
 $q_\theta(\mathbf{x}) \leftarrow \sum_{i=1}^r \eta_i \sqrt{w_{s_i}} [k_M(\mathbf{x}_{s_i}, \mathbf{x}) - k_M(\mathbf{y}_{s_i}, \mathbf{x})]$;
 // Update q_θ
 $M \leftarrow \sum_{n=1}^N \nabla q_\theta(\mathbf{x}_n) \nabla q_\theta(\mathbf{x}_n)^T$;
 // Update M
 end
 return M, q_θ

function and the approximation. Specifically, the change-of-basis $\mathbf{z} = M^{1/2}\mathbf{x}$ causes f_θ to have isotropic gradients $\nabla_{\mathbf{z}} f_\theta(\mathbf{z}_1), \dots, \nabla_{\mathbf{z}} f_\theta(\mathbf{z}_N)$. Thus, it becomes relatively easy to approximate f using a linear combination of isotropic kernel functions. See Appendix B for a proof of the isotropy property of the RFM.

The main contributions of this work are the extension of the RFM to the committor problem, together with an efficient strategy for optimizing the coefficient vector $\boldsymbol{\theta}$. In homage to the original RFM paper¹⁹, the new method is called the ‘‘fast committor machine’’ (FCM).

Pseudocode for the FCM is provided in Algorithm 1. As a helpful feature, the pseudocode normalizes the scaling matrix M by the trace of the covariance matrix

$$\begin{aligned} & \text{tr cov}(\{M^{1/2}\mathbf{x}_1, \dots, M^{1/2}\mathbf{x}_N\}) \\ &= \frac{1}{N(N-1)} \sum_{m,n=1}^N \|M^{1/2}(\mathbf{x}_m - \mathbf{x}_n)\|^2. \end{aligned}$$

This makes it easier to select and interpret the bandwidth parameter $\varepsilon > 0$. For the experiments in Sec. III, setting $\varepsilon = 1$ works well as a default.

D. Optimization of the coefficients $\boldsymbol{\theta}_n$

To derive an efficient procedure for optimizing the coefficient vector $\boldsymbol{\theta} \in \mathbb{R}^N$, the first step is to rewrite the optimization as a standard least-squares problem. To that end, rescale the coefficients according to

$$\bar{\boldsymbol{\theta}}_n = \boldsymbol{\theta}_n / \sqrt{w_n}, \quad n = 1, \dots, N.$$

Also, introduce the kernel matrix $\mathbf{K} \in \mathbb{R}^{N \times N}$ and the solution vector $\mathbf{b} \in \mathbb{R}^N$ have entries given by

$$\begin{aligned} k_{mn} &= \sqrt{w_m} \sqrt{w_n} [k_M(\mathbf{x}_m, \mathbf{x}_n) - k_M(\mathbf{x}_m, \mathbf{y}_n) \\ &\quad - k_M(\mathbf{y}_m, \mathbf{x}_n) + k_M(\mathbf{y}_m, \mathbf{y}_n)], \\ b_n &= \sqrt{w_n} [1_B(\mathbf{y}_n) - 1_B(\mathbf{x}_n)] \end{aligned}$$

Then, the optimal vector $\bar{\boldsymbol{\theta}} \in \mathbb{R}^N$ is the minimizer of the regularized least-square loss:

$$L_\gamma(\bar{\boldsymbol{\theta}}) = \frac{1}{N} \|\mathbf{K} \bar{\boldsymbol{\theta}} - \mathbf{b}\|^2 + \gamma \bar{\boldsymbol{\theta}}^T \mathbf{K} \bar{\boldsymbol{\theta}}. \quad (9)$$

Notice that the loss function (9) includes a regularization term $\gamma \bar{\boldsymbol{\theta}}^T \mathbf{K} \bar{\boldsymbol{\theta}}$ with $\gamma > 0$ that shrinks the norm of the coefficients to help prevent overfitting. Specifically, $(\bar{\boldsymbol{\theta}}^T \mathbf{K} \bar{\boldsymbol{\theta}})^{1/2}$ is the reproducing kernel Hilbert space (RKHS) norm associated with the committor approximation q_θ . RKHS norms appear frequently in the kernel literature due to their theoretical properties and computational convenience; see Sec. 2.3 of the paper⁴⁰ for an introduction.

For large data sets with $N \geq 10^5$ data points, it is computationally convenient to use a randomized strategy for solving

$$\min_{\bar{\boldsymbol{\theta}} \in \mathbb{R}^d} \frac{1}{N} \|\mathbf{K} \bar{\boldsymbol{\theta}} - \mathbf{b}\|^2 + \gamma \bar{\boldsymbol{\theta}}^T \mathbf{K} \bar{\boldsymbol{\theta}},$$

The randomly pivoted Cholesky algorithm (Algorithm 2) selects a set of ‘‘landmark’’ indices

$$S = \{s_1, s_2, \dots, s_r\}.$$

Then, the coefficient vector $\bar{\boldsymbol{\theta}} \in \mathbb{R}^N$ is restricted to satisfy $\bar{\boldsymbol{\theta}}_i = 0$ for all $i \notin S$ and

$$\bar{\boldsymbol{\theta}}(S) = \boldsymbol{\eta}.$$

Last, the vector $\boldsymbol{\eta} \in \mathbb{R}^r$ is optimized by solving

$$\min_{\boldsymbol{\eta} \in \mathbb{R}^r} \frac{1}{N} \|\mathbf{K}(:, S) \boldsymbol{\eta} - \mathbf{b}\|^2 + \gamma \boldsymbol{\eta}^T \mathbf{K}(S, S) \boldsymbol{\eta},$$

which is equivalent to the linear system

$$[\mathbf{K}(:, S)^T \mathbf{K}(:, S) + \gamma N \mathbf{K}(S, S)] \boldsymbol{\eta} = \mathbf{K}(:, S)^T \mathbf{b}.$$

It takes just $\mathcal{O}(Nr^2)$ operations to form and solve this linear system by a direct method. Moreover, there is no need to generate the complete kernel matrix $\mathbf{K} \in \mathbb{R}^{N \times N}$; it suffices to generate the r -column submatrix $\mathbf{K}(:, S)$, and the storage requirements are thus $\mathcal{O}(Nr)$.

Algorithm 2: RPCholesky²⁰

Data: Formula for looking up entries of \mathbf{K} , approximation rank r (multiple of 10);

Result: Index set S ;

Initialize: $\mathbf{F} \leftarrow \mathbf{0}$, $S \leftarrow \emptyset$, $T \leftarrow r/10$, and $\mathbf{d} \leftarrow \text{diag}(\mathbf{K})$;

// Initialize parameters

for $i = 0$ to 9 do

$s_{iT+1}, \dots, s_{iT+T} \sim \mathbf{d} / \sum_{j=1}^T d_j$;

// Randomly sample indices

$S' \leftarrow \text{Unique}(\{s_{iT+1}, \dots, s_{iT+T}\})$;

// Identify unique indices

$S \leftarrow S \cup S'$;

// Add new indices to landmark set

$\mathbf{G} \leftarrow \mathbf{K}(:, S') - \mathbf{F}\mathbf{F}(S', :)^*$;

// Evaluate new columns

$\mathbf{G}(S', :) \leftarrow \mathbf{G}(S', :) + \varepsilon_{\text{mach}} \text{tr}(\mathbf{G}(S', :)) \mathbf{I}$;

// Regularize

$\mathbf{R} \leftarrow \text{Cholesky}(\mathbf{G}(S', :))$;

// Upper triangular Cholesky factor

$\mathbf{F}(:, iT+1:iT+T+|S'|) \leftarrow \mathbf{G}\mathbf{R}^{-1}$;

// Update approximation

$\mathbf{d} \leftarrow \mathbf{d} - \text{SquaredRowNorms}(\mathbf{G}\mathbf{R}^{-1})$;

// Update sampling probabilities

$\mathbf{d} \leftarrow \max\{\mathbf{d}, 0\}$;

// Ensure nonnegative probabilities

$\mathbf{d}(S') \leftarrow 0$;

// Prevent double sampling

end

return S

E. Optimization of the hyperparameters

The last parameters to optimize are the bandwidth $\varepsilon > 0$, the regularization $\gamma > 0$, and the approximation rank r . To select these parameters, a simple but effective approach is a grid search. In the grid search, 10% of the data is set aside as validation data and the rest is training data. The FCM is optimized using the training data across various parameter combinations. Then the loss function (3) is evaluated using the validation data, and the best parameters are the ones that minimize the loss.

Based on the grid search results in Sec. III, a good default bandwidth is $\varepsilon = 1$. This bandwidth is intuitively reasonable, since it corresponds to one standard deviation unit for the transformed data points $\mathbf{M}^{1/2}\mathbf{x}_1, \dots, \mathbf{M}^{1/2}\mathbf{x}_n$.

Based on the grid search, the regularization parameter is set to $\gamma = 10^{-6}$, but this is not intuitive and it remains unclear whether this would be a good default for other problems. Any value of γ smaller than $\gamma = 10^{-6}$ also leads to a similar loss (less than 1% change in loss). To be conservative, the highest value $\gamma = 10^{-6}$ was selected.

The last parameter to optimize is the approximation rank r that is used in RPCholesky. Raising r increases the accuracy but also increases the linear algebra cost, since the FCM optimization requires $\mathcal{O}(Nr^2)$ floating point operations. Typical values of r range from 10^2 – 10^4 , and the theoretical optimum depends on the number of large eigenvalues in the full-data kernel matrix²⁰ which is not known in practice. In the Sec. III

experiments, the rank is set to $r = 10^3$, at which point the results are partially converged (see Fig. 3).

III. NUMERICAL RESULTS

This section describes numerical results from applying the fast committor machine (FCM) to two stochastic processes: the overdamped Langevin dynamics with a triple-well potential (Sec. III B) and a stochastic simulation of the alanine dipeptide miniprotein (Sec. III C). The code to run the experiments is available on Github⁴¹.

A. Neural network comparison

In each experiment, the FCM was compared against a fully connected feedforward neural network. To make the comparisons fair, the models were designed with a similar number of parameters. The FCM has r linear coefficients and $d(d+1)/2$ free parameters in the scaling matrix (d is the phase space dimension). This adds up to 1055 parameters for the triple-well experiment ($r = 1000$, $d = 10$) and 1465 parameters for the alanine dipeptide experiment ($r = 1000$, $d = 30$). The neural architecture includes M hidden layers with L neurons per layer and a tanh nonlinearity. The outer layer uses a sigmoid activation function to ensure the output lies between 0 and 1. The total number of parameters in the neural network is thus

$$M(d+1) + (L-1)M(M+1) + (M+1)$$

and includes 1081 parameters for the triple-well experiment ($L = 2$, $M = 27$, $d = 10$) and 1281 parameters for the alanine dipeptide experiment ($L = 3$, $M = 20$, $d = 30$). Larger neural net models could potentially improve the accuracy⁴², but they would also be more challenging and costly to train.

The neural nets were trained using the PyTorch package⁴³ and the AdamW optimizer⁴⁴. Before the training, 20% of the data was set aside for validation, and the remaining 80% was used as training data. During each epoch of training time, the optimizer evaluated all the training data and applied stochastic gradient updates calculated from mini-batches of 500 points. After each epoch, the parameter values were saved and the validation data was used to estimate the loss function (3). After 20 epochs with no improvement to the loss function, the training halted and the best parameter set was used.

One crucial parameter when training neural nets is the learning rate, which was set to 10^{-4} for the triple-well experiment and 5×10^{-4} for the alanine dipeptide experiment. When the learning rate is too small, the training is excessively slow. When the learning rate is too large, the model exhibits a significant decrease in accuracy or even fails to converge. Additionally, changing the learning rate may make it necessary to change the patience parameter (number of epochs with no improvement before halting the training).

On the whole, training neural networks for committor approximation involves choosing an appropriate architecture and an appropriate learning rate with minimal guidance about

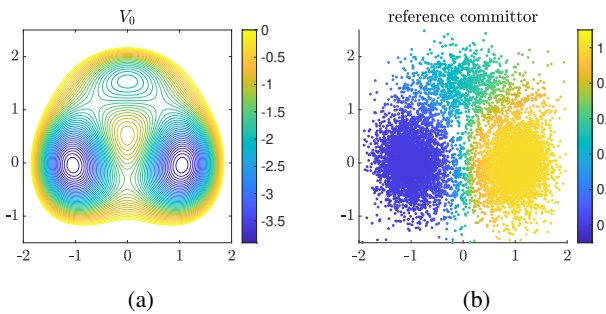


FIG. 1: (a) The potential function V_0 . (b) The reference committor evaluated on the validation data points.

the best choice of these parameters. In contrast, the parameter-tuning for the FCM is more straightforward: *every* choice of parameters produced a stable committor approximation in the experiments, and adjusting the approximation rank r and regularization parameter γ only served to heighten the approximation accuracy.

B. Triple-well potential energy

The first numerical test is based on the overdamped Langevin dynamics

$$d\mathbf{x}(t) = -\nabla V(\mathbf{x}(t))dt + \sqrt{2\beta^{-1}}d\mathbf{w}(t). \quad (10)$$

The potential function $V(x)$ is constructed as

$$V(\mathbf{x}) = V_0(e_1^T \mathbf{x}, e_2^T \mathbf{x}) + 2 \sum_{i=3}^{10} (e_i^T \mathbf{x})^2,$$

where V_0 is the standard three-well potential¹¹ that is illustrated in Figure 1, and e_i is the i th basis vector. The equilibrium density for this process is the Gibbs measure

$$\mu(\mathbf{x}) = \frac{e^{-\beta V(\mathbf{x})}}{\int e^{-\beta V(\mathbf{y})} d\mathbf{y}},$$

where $\beta > 0$ is the inverse-temperature parameter.

The goal of this test is to calculate the committor function associated with the inverse temperature $\beta = 2$ and the states

$$A = \{\mathbf{x} \in \mathbb{R}^{10} : (e_1^T \mathbf{x} + 1)^2 + (e_2^T \mathbf{x})^2 \leq 0.3^2\},$$

$$B = \{\mathbf{x} \in \mathbb{R}^{10} : (e_1^T \mathbf{x} - 1)^2 + (e_2^T \mathbf{x})^2 \leq 0.3^2\}.$$

The definitions for A and B depend only on coordinates 1 and 2. Coordinates 3–10 are nuisance coordinates which have no effect on the committor but increase difficulty of the committor approximation. Nonetheless, because the committor only depends on coordinates 1 and 2, the finite elements method can solve the two-dimensional PDE formulation of the committor problem to generate a highly accurate reference. See Figure 1 for an illustration of the reference committor.

The data set was generated by a two-phase process. In the first phase, initial states $(\mathbf{x}_n)_{1 \leq n \leq N}$ were sampled by running

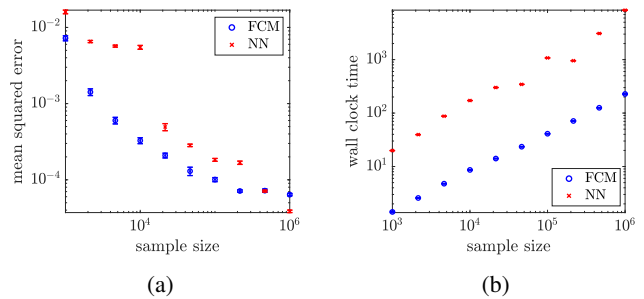


FIG. 2: Comparison of neural net (NN) and FCM performance for the triple-well system, with standard error bars computed from 10 independent runs of the FCM. (a) Mean squared error computed using the reference committor. (b) Runtime in seconds.

the Langevin dynamics (10) at the inverse temperature $\beta_s = 1$ and storing the positions after $N = 10^6$ uniformly spaced time intervals. The low β_s value was designed to ensure adequate phase space coverage. Since the sampling distribution diverges from the target distribution, the initial states were weighted according to $w_n = e^{(\beta_s - \beta)V(\mathbf{x}_n)}$.

In the second phase, the process was simulated for an additional $\tau = 10^{-2}$ time units at the target inverse temperature $\beta = 2$, starting from $\mathbf{x}(0) = \mathbf{x}_n$ and ending at a new point $\mathbf{x}(\tau) = \mathbf{y}_n$. This process was repeated for each data point for $n = 1, \dots, 10^6$.

Figure 2 evaluate the performance of the FCM and the feedforward neural network across 10 data sizes, logarithmically spaced between $N = 10^3$ and $N = 10^6$. The largest experiments use the full data set with $N = 10^6$ data points, while the other experiments use fewer data pairs chosen uniformly at random. For all sample sizes $N < 10^6$, the FCM achieves higher accuracy than the neural net and also trains more quickly.

The detailed runtime and accuracy comparisons between the FCM and the neural net committor approximation may depend on implementation choices (neural net structure, stopping criteria, optimization method, etc.). Nonetheless, these tests suggest that the FCM is truly a competitive method for the triple-well committor calculation.

As an additional advantage, the FCM exhibits robustness during training. Figure 3 shows that the FCM error decreases and then stabilizes after a few iterations, especially when using a large approximation rank $r \geq 400$. In contrast, the neural net error behaves unpredictably with epochs. To interpret the plot, recall that the FCM updates the scaling matrix \mathbf{M} once per iteration and runs for 5 iterations, while the neural net updates the neural net parameters many times per epoch and runs for a variable number of epochs based on the stopping rule.

Last, Figure 4 shows that the square root of the scaling matrix encodes interpretable information about which subspaces are maximally important for committor estimation. After convergence, the transformation $\mathbf{M}^{1/2}$ maps away the nuisance coordinates 3–10. The leading eigenvector of $\mathbf{M}^{1/2}$ nearly aligns with coordinate 1, signaling that coordinate 1 is the

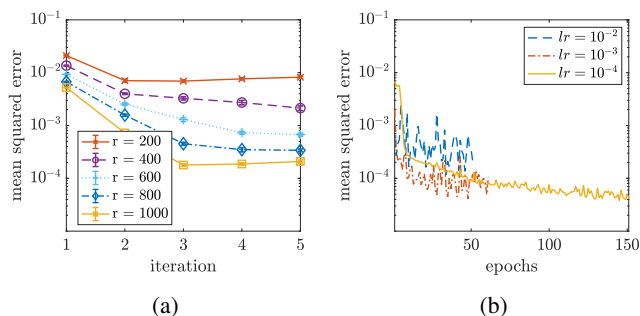


FIG. 3: Training performance for the triple-well experiment, with error computed using the reference committor from Fig. 1. (a) The FCM with different approximation ranks r . (b) The neural net with different learning rates lr .

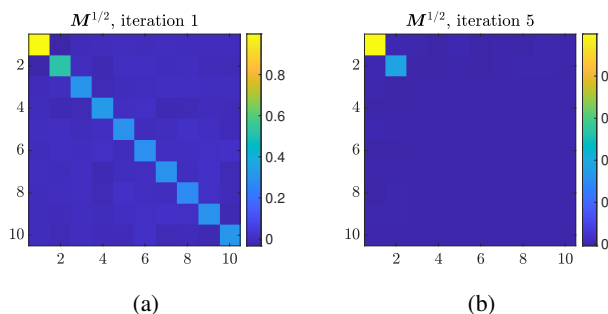


FIG. 4: Square root of scaling matrix for the triple-well system when $N = 10^6$ and $r = 1000$. (a) After 1 iteration. (b) After 5 iterations, corresponding to convergence.

most essential for committor estimation and coordinate 2 is the second most essential. While the two-dimensional figures make it seem that the FCM is solving an easy problem in two-dimensional space, the FCM is actually solving a harder problem in ten-dimensional space. Nonetheless, the FCM is reducing the problem to two dimensions through the automatic identification of the active subspaces.

C. Alanine dipeptide

The previous example may seem cherry-picked for the FCM's success, since there is so clearly a reduction to two dimensions. Yet low-dimensional subspaces can frequently be harnessed in stochastic analysis, including the analysis of high-dimensional biomolecules⁴⁵. As another example, the alanine dipeptide is a well known miniprotein whose dynamics can be reduced to a low-dimensional subspace.

The experiments in this section are drawn from a metadynamics simulation of alanine dipeptide based on the tutorial⁴⁶. Details of the simulation can be found on Github⁴⁷. After excluding the hydrogen atoms, the data set contains (x, y, z) -coordinates for the ten backbone atoms of the alanine dipeptide, so the molecule can be viewed as a stochastic process in \mathbb{R}^{30} . Nonetheless, Figure 5 shows that ϕ and ψ di-

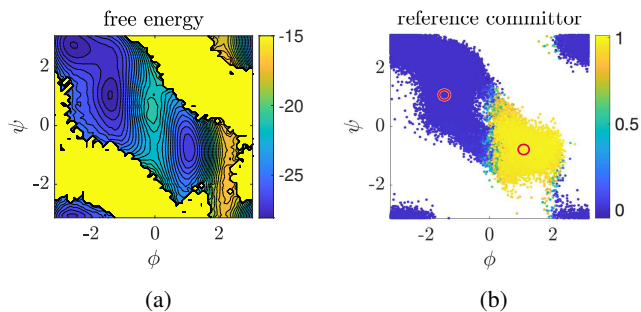


FIG. 5: (a) Free energy surface of alanine dipeptide in ϕ and ψ coordinates. (b) The reference committor in ϕ and ψ coordinates. States A and B are circled.

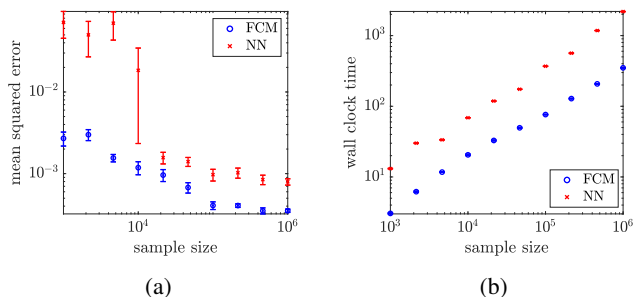


FIG. 6: Comparison of neural net (NN) and FCM performance for alanine dipeptide, with standard error bars computed from 10 independent simulations. (a) Mean squared error, computed with respect to the reference. (b) Runtime in seconds.

edral angles give a simple description of the free energy surface, emphasizing two metastable states.

The goal of this experiment is to estimate the committor function for the two metastable states, labeled as A and B. See Figure 5 for a picture of the precise A and B definitions and a reference committor which is generated by running the FCM with the largest data set ($N = 10^6$) and largest approximation rank ($r = 2000$).

Figure 6 shows the mean squared error and runtimes of the FCM and neural network, compared to the reference committor. The results again show the FCM is more accurate than the neural network and runs more quickly. These results may depend sensitively on the details of the neural network optimization, but they imply the FCM is a competitive method for the alanine dipeptide experiment.

Last, Figure 7 shows the square root of the FCM scaling matrix along with the 10 largest eigenvalues of the matrix. The comparison reveals that 2 eigenvalues are much larger than the rest, signaling that a two-dimensional linear subspace is especially adapted to the committor problem with sets A and B. Linear regression confirms that these top 2 eigenvectors explain 95% of the variance in the committor values, whereas the nonlinear ϕ and ψ coordinates only explain 62% of the variance. See the bottom panel of Fig. 7 for a picture of the

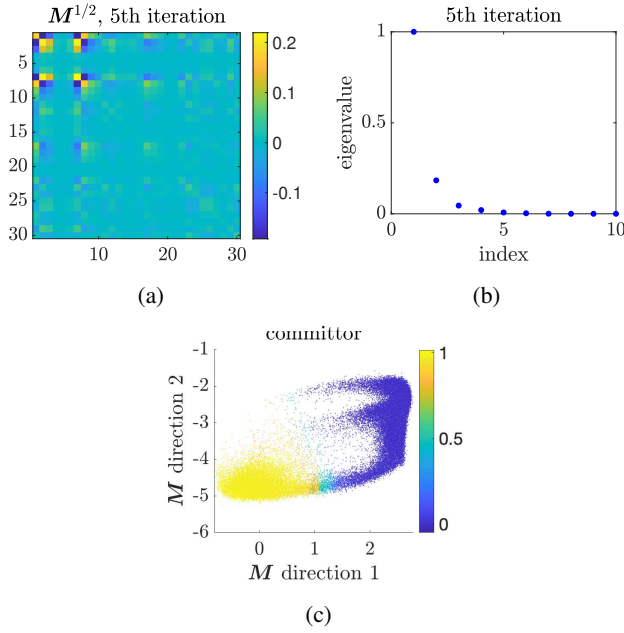


FIG. 7: Results of applying FCM to alanine dipeptide when $N = 10^6$ and $r = 1000$. (a) $M^{1/2}$ after 5 iterations of Algorithm 1, corresponding to convergence. (b) Top 10 eigenvalues of $M^{1/2}$. (c) Reference committor mapped onto top 2 eigenvectors of M .

reference committor mapped onto the top 2 eigenvectors.

IV. CONCLUSION

The FCM is a method for efficiently solving the committor problem which shows promising results when applied to triple-well and alanine dipeptide systems. As the main conceptual feature, the method adaptively identifies a scaling matrix which emphasizes low-dimensional subspaces with maximal variation in the committor values. Moving forward, the FCM should be tested on higher-dimensional stochastic systems emerging in molecular dynamics and beyond.

From a mathematical perspective, there remain several challenging questions about the FCM's performance. These include understanding why the method takes so few iterations to successfully converge and what makes the exponential kernel (6) preferable over the square exponential kernel and other choices. Last, there is the deep question about why the linear rescaling is so successful, how to describe it mathematically, and what nonlinear extensions would be possible.

Appendix A: Justification for the kernel approximation

The FCM is based on a few specific choices regarding the shape of the kernel function (square exponential versus exponential) and the coefficients used in the optimization. This appendix justifies the choices that were made.

In the Sec. III experiments, the exponential kernel (6) outperforms the popular square exponential kernel

$$k_M(\mathbf{x}, \mathbf{x}') = \exp(-\varepsilon^{-2} \|\mathbf{M}^{1/2}(\mathbf{x} - \mathbf{x}')\|^2).$$

Therefore, the exponential kernel is used throughout this work. Nonetheless, there may be an opportunity for a further improvements to the FCM through a more general kernel of the form

$$k_M(\mathbf{x}, \mathbf{x}') = \phi(\varepsilon^{-1} \|\mathbf{M}^{1/2}(\mathbf{x} - \mathbf{x}')\|)$$

for some decreasing univariate function $\phi : \mathbb{R} \rightarrow \mathbb{R}$.

A kernel approximation consists of linear combinations of kernel functions centered on the data points, so the most general formulation is

$$q_{\mathbf{c}, \mathbf{d}}(\mathbf{x}) = \sum_{n=1}^N c_n k_M(\mathbf{x}_n, \mathbf{x}) + \sum_{n=1}^N d_n k_M(\mathbf{y}_n, \mathbf{x}),$$

where $\mathbf{c} \in \mathbb{R}^N$ and $\mathbf{d} \in \mathbb{R}^N$ are variational parameters to be optimized. Surprisingly, Theorem A.1 shows that the optimal coefficients must satisfy $\mathbf{c} = -\mathbf{d}$, which leads to a more specific committor approximation

$$q_{\theta}(\mathbf{x}) = \sum_{n=1}^N \theta_n [k_M(\mathbf{x}_n, \mathbf{x}) - k_M(\mathbf{y}_n, \mathbf{x})].$$

The proof relies on an explicit coefficient optimization using linear algebra.

Theorem A.1. *Define the least-squares loss function*

$$L_{\gamma}(\mathbf{c}, \mathbf{d}) = \frac{1}{N} \left\| \begin{bmatrix} \mathbf{I} \\ -\mathbf{I} \end{bmatrix}^T \mathbf{K} \begin{bmatrix} \mathbf{c} \\ \mathbf{d} \end{bmatrix} - \mathbf{b} \right\|^2 + \gamma \begin{bmatrix} \mathbf{c} \\ \mathbf{d} \end{bmatrix}^T \mathbf{K} \begin{bmatrix} \mathbf{c} \\ \mathbf{d} \end{bmatrix},$$

where the positive semidefinite kernel matrix

$$\mathbf{K} = \begin{bmatrix} \mathbf{K}^{11} & \mathbf{K}^{12} \\ \mathbf{K}^{21} & \mathbf{K}^{22} \end{bmatrix},$$

consists of four blocks with entries

$$\begin{aligned} k_{mn}^{11} &= \sqrt{w_m} \sqrt{w_n} k_M(\mathbf{x}_m, \mathbf{x}_n), \\ k_{mn}^{12} &= \sqrt{w_m} \sqrt{w_n} k_M(\mathbf{x}_m, \mathbf{y}_n), \\ k_{mn}^{21} &= \sqrt{w_m} \sqrt{w_n} k_M(\mathbf{y}_m, \mathbf{x}_n), \\ k_{mn}^{22} &= \sqrt{w_m} \sqrt{w_n} k_M(\mathbf{y}_m, \mathbf{y}_n). \end{aligned}$$

Then, the loss function $L_{\gamma}(\mathbf{c}, \mathbf{d})$ has a minimizer that satisfies $\mathbf{c} + \mathbf{d} = \mathbf{0}$.

Proof. The loss function is convex, so any minimizers can be identified by setting the gradient equal to zero:

$$\frac{2}{N} \mathbf{K} \begin{bmatrix} \mathbf{I} \\ -\mathbf{I} \end{bmatrix} \left[\begin{bmatrix} \mathbf{I} \\ -\mathbf{I} \end{bmatrix}^T \mathbf{K} \begin{bmatrix} \mathbf{c} \\ \mathbf{d} \end{bmatrix} - \mathbf{b} \right] + 2\gamma \mathbf{K} \begin{bmatrix} \mathbf{c} \\ \mathbf{d} \end{bmatrix} = \mathbf{0}.$$

The equation can be rearranged to yield

$$\mathbf{K} \begin{bmatrix} \mathbf{I} \\ -\mathbf{I} \end{bmatrix} \begin{bmatrix} \mathbf{I} \\ -\mathbf{I} \end{bmatrix}^T \mathbf{K} + \gamma N \begin{bmatrix} \mathbf{I} & \\ & \mathbf{I} \end{bmatrix} \begin{bmatrix} \mathbf{c} \\ \mathbf{d} \end{bmatrix} = \mathbf{K} \begin{bmatrix} \mathbf{I} \\ -\mathbf{I} \end{bmatrix} \mathbf{b}$$

Therefore, there is a minimizer which comes from choosing \mathbf{c} and \mathbf{d} to satisfy the positive definite linear system

$$\begin{bmatrix} \mathbf{I} \\ -\mathbf{I} \end{bmatrix} \begin{bmatrix} \mathbf{I} \\ -\mathbf{I} \end{bmatrix}^T \mathbf{K} + \gamma^N \begin{bmatrix} \mathbf{I} \\ \mathbf{I} \end{bmatrix} \begin{bmatrix} \mathbf{c} \\ \mathbf{d} \end{bmatrix} = \begin{bmatrix} \mathbf{I} \\ -\mathbf{I} \end{bmatrix} \mathbf{b}. \quad (\text{A1})$$

(All other minimizers come from adding a vector in the nullspace of \mathbf{K}). Last, multiply the system (A1) on the left by $\begin{bmatrix} \mathbf{I} & \mathbf{I} \end{bmatrix}$ to reveal $\mathbf{c} + \mathbf{d} = \mathbf{0}$. \square

Appendix B: The scaling matrix

In any learning task, it can be helpful to model a function $f: \mathbb{R}^d \rightarrow \mathbb{R}$ as the composition of an invertible linear map $\mathbf{A}: \mathbb{R}^d \rightarrow \mathbb{R}^d$ with a function $g_{\mathbf{A}}$ that is relatively easy to learn:

$$f(\mathbf{x}) = g_{\mathbf{A}}(\mathbf{A}\mathbf{x}), \quad \mathbf{x} \in \mathbb{R}^d.$$

One way to ensure the learnability of the function $g_{\mathbf{A}}$ is by selecting the matrix \mathbf{A} so that the gradients

$$\nabla g_{\mathbf{A}}(\mathbf{z}_1), \dots, \nabla g_{\mathbf{A}}(\mathbf{z}_N)$$

are isotropic, where

$$\mathbf{z}_i = \mathbf{A}\mathbf{x}_i, \quad i = 1, 2, \dots, N$$

are the linearly transformed data points. The optimal transformation can be characterized as follows:

Proposition B.1. *The following are equivalent:*

(i) \mathbf{A} is invertible, and the sample gradients $\nabla g_{\mathbf{A}}(\mathbf{z}_1), \dots, \nabla g_{\mathbf{A}}(\mathbf{z}_N)$ are isotropic, that is,

$$\frac{1}{N} \sum_{i=1}^N |\mathbf{u}^T \nabla g_{\mathbf{A}}(\mathbf{z}_i)|^2 = 1$$

for any unit vector $\mathbf{u} \in \mathbb{R}^d$.

(ii) The average gradient product

$$\mathbf{M} = \frac{1}{N} \sum_{i=1}^N \nabla f(\mathbf{x}_i) \nabla f(\mathbf{x}_i)^T.$$

is invertible, and $\mathbf{A} = \mathbf{Q}\mathbf{M}^{1/2}$ for an orthogonal matrix $\mathbf{Q} \in \mathbb{R}^{d \times d}$.

(iii) \mathbf{M} is invertible, and \mathbf{A} transforms distances according to

$$\|\mathbf{A}(\mathbf{x} - \mathbf{x}')\| = \|\mathbf{M}^{1/2}(\mathbf{x} - \mathbf{x}')\|,$$

for each $\mathbf{x}, \mathbf{x}' \in \mathbb{R}^d$.

Proof. Either of the conditions (i)-(ii) implies the linear map \mathbf{A} is invertible. Therefore calculate

$$\begin{aligned} \frac{1}{N} \sum_{i=1}^N |\mathbf{u}^T \nabla g_{\mathbf{A}}(\mathbf{z}_i)|^2 &= \frac{1}{N} \sum_{i=1}^N |\mathbf{u}^T \mathbf{A}^{-T} \nabla f(\mathbf{x}_i)|^2 \\ &= \mathbf{u}^T \mathbf{A}^{-T} \mathbf{M} \mathbf{A}^{-1} \mathbf{u}. \end{aligned}$$

The above display is 1 for each unit vector $\mathbf{u} \in \mathbb{R}^d$ if and only if $\mathbf{A}^{-T} \mathbf{M} \mathbf{A}^{-1} = \mathbf{I}$ and $\mathbf{M}^{1/2} \mathbf{A}^{-1}$ is an orthogonal matrix. Thus, (i) and (ii) are equivalent.

Clearly, (ii) implies (iii). Conversely, if $\|\mathbf{A}\mathbf{x}\| = \|\mathbf{M}^{1/2}\mathbf{x}\|$ for each $\mathbf{x} \in \mathbb{R}^d$, it follows that

$$\mathbf{M} = \mathbf{A}^T \mathbf{A}.$$

Consequently, if $\mathbf{A} = \mathbf{U}\Sigma\mathbf{V}^T$ is a singular value decomposition for \mathbf{A} , then $\mathbf{M} = \mathbf{V}\Sigma^2\mathbf{V}^T$ is an eigenvalue decomposition for \mathbf{M} , and

$$\mathbf{A} = \mathbf{Q}\mathbf{M}^{1/2}, \quad \text{where } \mathbf{Q} = \mathbf{U}\mathbf{V}^T \text{ is orthogonal.} \quad (\text{B1})$$

This shows that (ii) and (iii) are equivalent. \square

- ¹K. A. Newhall and E. Vanden-Eijnden, *Journal of Nonlinear Science* **27**, 1007 (2017).
- ²T. Grafke and E. Vanden-Eijnden, *Chaos: An Interdisciplinary Journal of Nonlinear Science* **29**, 063118 (2019), publisher: American Institute of Physics.
- ³V. Jacques-Dumas, R. M. van Westen, F. Bouchet, and H. A. Dijkstra, *Nonlinear Processes in Geophysics* **30**, 195 (2023), publisher: Copernicus GmbH.
- ⁴D. Lucente, C. Herbert, and F. Bouchet, *Journal of the Atmospheric Sciences* **79**, 2387–2400 (2022).
- ⁵P. G. Bolhuis, D. Chandler, C. Dellago, and P. L. Geissler, *Annual Review of Physical Chemistry* **53**, 291 (2002).
- ⁶J. Rogal and P. G. Bolhuis, *The Journal of Chemical Physics* **129**, 224107 (2008).
- ⁷R. J. Allen, D. Frenkel, and P. R. ten Wolde, *The Journal of Chemical Physics* **124**, 194111 (2006).
- ⁸F. A. Escobedo, E. E. Borrero, and J. C. Araque, *Journal of Physics: Condensed Matter* **21**, 333101 (2009).
- ⁹W. E, W. Ren, and E. Vanden-Eijnden, *The Journal of Physical Chemistry B* **109**, 6688 (2005), publisher: American Chemical Society.
- ¹⁰E. Vanden-Eijnden and M. Venturoli, *The Journal of Chemical Physics* **130**, 194103 (2009).
- ¹¹F. Cérou, A. Guyader, T. Lelièvre, and D. Pommier, *The Journal of Chemical Physics* **134**, 054108 (2011).
- ¹²Y. Khoo, J. Lu, and L. Ying, *Research in the Mathematical Sciences* **6**, 1 (2019).
- ¹³R. Lai and J. Lu, *Multiscale Modeling & Simulation* **16**, 710 (2018).
- ¹⁴D. Lucente, J. Rolland, C. Herbert, and F. Bouchet, arXiv:2110.05050 [cond-mat, physics:physics] (2021), arXiv: 2110.05050.
- ¹⁵Q. Li, B. Lin, and W. Ren, *The Journal of Chemical Physics* **151** (2019), 10.1063/1.5110439.
- ¹⁶L. Evans, M. K. Cameron, and P. Tiwary, *The Journal of Chemical Physics* **157**, 214107 (2022).
- ¹⁷A. M. Berezhkovskii and A. Szabo, *The Journal of Chemical Physics* **150**, 054106 (2019), publisher: American Institute of Physics.
- ¹⁸H. Li, Y. Khoo, Y. Ren, and L. Ying, in *Proceedings of the 2nd Mathematical and Scientific Machine Learning Conference* (PMLR, 2022) pp. 598–618, iSSN: 2640-3498.
- ¹⁹A. Radhakrishnan, D. Beaglehole, P. Pandit, and M. Belkin, arXiv preprint arXiv:2212.13881 (2022).
- ²⁰Y. Chen, E. N. Epperly, J. A. Tropp, and R. J. Webber, “Randomly pivoted Cholesky: Practical approximation of a kernel matrix with few entry evaluations,” (2023), arXiv:2207.06503 [cs, math, stat].
- ²¹V. L. Deringer, A. P. Bartók, N. Bernstein, D. M. Wilkins, M. Ceriotti, and G. Csányi, *Chemical Reviews* **121**, 10073 (2021).
- ²²F. Musil, A. Grisafi, A. P. Bartók, C. Ortner, G. Csányi, and M. Ceriotti, *Chemical Reviews* **121**, 9759 (2021).
- ²³R. R. Coifman, I. G. Kevrekidis, S. Lafon, M. Maggioni, and B. Nadler, *Multiscale Modeling & Simulation* **7**, 23 (2008), num Pages: 23 Place: Philadelphia, United States Publisher: Society for Industrial and Applied Mathematics.
- ²⁴F. Noé and F. Nüske, *Multiscale Modeling & Simulation* **11**, 635 (2013).

- ²⁵H. Chen, B. Roux, and C. Chipot, *Journal of Chemical Theory and Computation* **19**, 4414 (2023).
- ²⁶C. Schütte, S. Klus, and C. Hartmann, *Acta Numerica* **32**, 517–673 (2023).
- ²⁷H. Chen and C. Chipot, *QRB Discovery* **4**, e2 (2023).
- ²⁸Y. Kamada and S. Abe, in *IAPR Workshop on Artificial Neural Networks in Pattern Recognition* (2006).
- ²⁹G. Camps-Valls, A. Rodrigo-Gonzalez, J. Munoz-Mari, L. Gomez-Chova, and J. Calpe-Maravilla, in *IEEE International Geoscience and Remote Sensing Symposium* (2007) pp. 3802–3805.
- ³⁰Q. Wu, J. Guinney, M. Maggioni, and S. Mukherjee, *Journal of Machine Learning Research* **11**, 2175 (2010).
- ³¹S. Trivedi, J. Wang, S. Kpotufe, and G. Shakhnarovich, in *Proceedings of the Thirtieth Conference on Uncertainty in Artificial Intelligence* (2014).
- ³²O. T. Unke, S. Chmiela, H. E. Sauceda, M. Gastegger, I. Poltavsky, K. T. Schütt, A. Tkatchenko, and K.-R. Müller, *Chemical Reviews* **121**, 10142 (2021).
- ³³C. K. I. Williams and M. Seeger, in *Proceedings of the 13th International Conference on Neural Information Processing Systems* (2000).
- ³⁴A. Rudi, L. Carratino, and L. Rosasco, in *Proceedings of the 31st International Conference on Neural Information Processing Systems* (2017).
- ³⁵Y. Chen, J. Hoskins, Y. Khoo, and M. Lindsey, *Journal of Computational Physics* **472**, 111646 (2023).
- ³⁶P. Doyle and J. Snell, *Random Walks and Electric Networks* (American Mathematical Society, 1984).
- ³⁷R. Hersh and R. J. Griego, *Scientific American* **220**, 66 (1969).
- ³⁸B. Schmuland, *The Canadian Journal of Statistics / La Revue Canadienne de Statistique* **27**, 683 (1999).
- ³⁹A. Radhakrishnan, M. Belkin, and D. Drusvyatskiy, arXiv:2401.04553 (2024).
- ⁴⁰M. Kanagawa, P. Hennig, D. Sejdinovic, and B. K. Sriperumbudur, “Gaussian processes and kernel methods: A review on connections and equivalences,” (2018), arXiv:1807.02582 [stat.ML].
- ⁴¹https://github.com/davidaristoff/FFM_committor.
- ⁴²M. Belkin, D. Hsu, S. Ma, and S. Mandal, *Proceedings of the National Academy of Sciences* **116**, 15849 (2019).
- ⁴³A. Paszke, S. Gross, F. Massa, A. Lerer, J. Bradbury, G. Chanan, T. Killeen, Z. Lin, N. Gimelshein, L. Antiga, A. Desmaison, A. Kopf, E. Yang, Z. DeVito, M. Raison, A. Tejani, S. Chilamkurthy, B. Steiner, L. Fang, J. Bai, and S. Chintala, arXiv preprint arXiv:1912.01703 (2019).
- ⁴⁴I. Loshchilov and F. Hutter, in *Proceedings of the Seventh International Conference on Learning Representations (ICLR)* (2019).
- ⁴⁵B. E. Husic and V. S. Pande, *Journal of the American Chemical Society* **140**, 2386 (2018).
- ⁴⁶<https://www.plumed.org/doc-v2.7/user-doc/html/masterclass-21-4.html>.
- ⁴⁷https://github.com/davidaristoff/FFM_committor.